

Second-harmonic mode coupling in microresonator-based optical frequency comb generation

Xiaoxiao Xue^{1,2*}, François Leo^{3,4}, Yi Xuan^{2,5}, Jose A. Jaramillo-Villegas^{2,6}, Pei-Hsun Wang², Daniel E. Leaird², Miro Erkintalo³, Minghao Qi^{2,5}, and Andrew M. Weiner^{2,5}

¹*Department of Electronic Engineering, Tsinghua University, Beijing 100084, China*

²*School of Electrical and Computer Engineering, Purdue University, 465 Northwestern Avenue, West Lafayette, Indiana 47907-2035, USA*

³*The Dodd-Walls Centre for Photonic and Quantum Technologies, Department of Physics, The University of Auckland, Auckland 1142, New Zealand*

⁴*OPERA-photonics, Université libre de Bruxelles (U.L.B.), 50 Avenue F. D. Roosevelt, CP 194/5, B-1050 Bruxelles, Belgium*

⁵*Birck Nanotechnology Center, Purdue University, 1205 West State Street, West Lafayette, Indiana 47907, USA*

⁶*Facultad de Ingenierías, Universidad Tecnológica de Pereira, Pereira, RIS 660003, Colombia*

[*xuexx@tsinghua.edu.cn](mailto:xuexx@tsinghua.edu.cn)

ABSTRACT

Simultaneous second-harmonic generation in microresonator-based Kerr optical frequency combs (microcombs) can potentially facilitate on-chip comb self-referencing for optical frequency metrology. Moreover, the participation of second-order nonlinearity may affect the comb self-starting and mode-locking behaviors, resulting in complex dynamics that is still far from well understood. Here, we report on both experimental and theoretical investigations on the interaction dynamics between the fundamental and second-harmonic waves in microcomb generation. We show that the nonlinear dynamics governed by the third-order nonlinearity can be significantly altered by the nonlinear mode coupling. Specifically, we demonstrate that second-harmonic mode coupling can provide an entirely new way of fulfilling phase-matching for four-wave mixing in the normal dispersion regime, where comb creation is prohibited in the absence of mode coupling. We derive coupled time-domain mean-field equations to model the comb dynamics in microresonators with simultaneous second- and third-order nonlinearities. The numerical simulation results show excellent agreement with our experimental observations. We expect our findings will have a wide impact on the study of nonlinear cavity dynamics with interacting second- and third-order nonlinearities, and will enable new mechanisms for reliable high-performance microcombs.

I. INTRODUCTION

Microresonator-based optical frequency comb (microcomb) generation is a technique that converts a single-frequency laser pump to a broadband comb source using a high-quality-factor microresonator [1]–[9]. The basic mechanism is based on cavity enhanced Kerr effect which is a kind of third-order nonlinearity. Microcomb generation is now a hot research area, not only because it provides a good platform for studying nonlinear optics, but also due to its attractive features for portable applications, mainly including the potential to achieve low power consumption and on-chip integration. Rich dynamics in the comb generation process has been observed, such as chaos [10], mode-locking [11]–[16], temporal bright and dark solitons [17]–[20], discrete phase steps [21], Cherenkov radiation [22], etc. Recently, simultaneous comb formation and second-harmonic generation were also observed in microresonators with both second- and third-order nonlinearities [23],[24]. In these systems, the role of the second-order nonlinearity has, however, been limited to the intracavity conversion of a Kerr microcomb to

other spectral regions, without influencing the comb formation dynamics itself. Nevertheless, second-harmonic generation could potentially facilitate on-chip comb self-referencing for optical frequency metrology when the comb spectra span over one octave [25]. Compared to a purely third-order system, the participation of second-order nonlinearity also brings new dynamics that is far from well understood [26]–[29].

In this work, we report a nonlinear mode coupling mechanism which can significantly change the comb dynamics in microresonators with both second- and third-order nonlinearities. The mode coupling arises from the interaction between the fundamental and the second-harmonic waves, and permits modulational instability in the normal-dispersion region where comb formation is typically prohibited in the absence of mode coupling. In both experiments and numerical simulations, we demonstrate broadband mode-locked comb generation in a microresonator which shows normal group velocity dispersion for the fundamental wave. Our work reveals, for the first time to our knowledge, that second-harmonic mode coupling can provide an entirely new way of fulfilling phase-matching for four-wave mixing in the normal dispersion regime, and may also alter the nonlinear dynamics in the anomalous dispersion regime. Compounded by the fact that second-order nonlinearity has been found in a number of microresonators currently exploited for comb generation [23],[24], our findings suggest that nonlinear mode coupling is an important factor that should be considered in the microresonator design, and that may enable new regions for microcomb generation.

II. EXPERIMENTAL RESULTS

A. Second-harmonic assisted comb generation

The microresonator we use is a silicon nitride (SiN) microring embedded in silicon dioxide; this is one of the microrings used in our previous report on mode-locked dark pulses [19]. Although second-order nonlinearity is absent in bulk amorphous SiN material, it can exist in SiN thin films and waveguides due to surface effects or due to silicon nanocrystals formed in the fabrication process [30]–[34]. Indeed, in our experiments we find that selected cavity resonances yield significant generation of light at the second-harmonic of the pump laser. A detailed schematic of our experimental setup for comb generation is shown in Fig. 1(a). An infrared (IR) tunable laser source in the C-band is amplified and pumps the SiN microring. The microring has a radius of 100 μm corresponding to a free spectral range (FSR) of ~ 231 GHz, and a loaded quality factor of 8.6×10^5 . The cross-section of the microring waveguide is $2 \mu\text{m} \times 550 \text{ nm}$, and its measured group velocity dispersion in the C-band is $186.9 \text{ ps}^2/\text{km}$, i.e., strongly normal. Both a through-port waveguide and a drop-port waveguide coupled to the microring are fabricated. The light from the microring chip is split into three branches. From top to bottom, the first branch measures the total power in the fundamental IR spectral range; the second branch measures the IR comb power excluding the pump line (the pulse shaper acts as a band-reject filter); the third branch measures the second-harmonic power (the IR power is blocked by a glass filter). The Pound–Drever–Hall (PDH) signal is also measured to monitor the effective pump-resonance detuning when the optical signal is analyzed at the through port [17] (setup not shown).

To generate a frequency comb, the wavelength of the pump laser is tuned around 1543 nm. Specifically, the laser sweeps from shorter wavelength to longer wavelength across the microring resonance at a relatively slow speed of 0.5 nm/s. The on-chip pump power is around 0.4 W. Figure 1(b) shows the transmission curves measured at the output of the microring chip, with the zoom-in details shown in Fig. 1(c). Due to the resonance shift caused by the Kerr and thermo-optic effects, the total power transmission has a typical triangular shape [35]. Furthermore, a signal at the second-harmonic can readily be detected as the pump laser tunes into resonance. Transition steps, which correspond to switching of the comb dynamics, can also be clearly observed in transmission curves corresponding to both the fundamental and the second-harmonic wavelengths. The PDH signal shown in the bottom panel of Fig. 1(b) indicates that the pump laser in comb operation is always effectively blue detuned with respect to the shifted resonance.

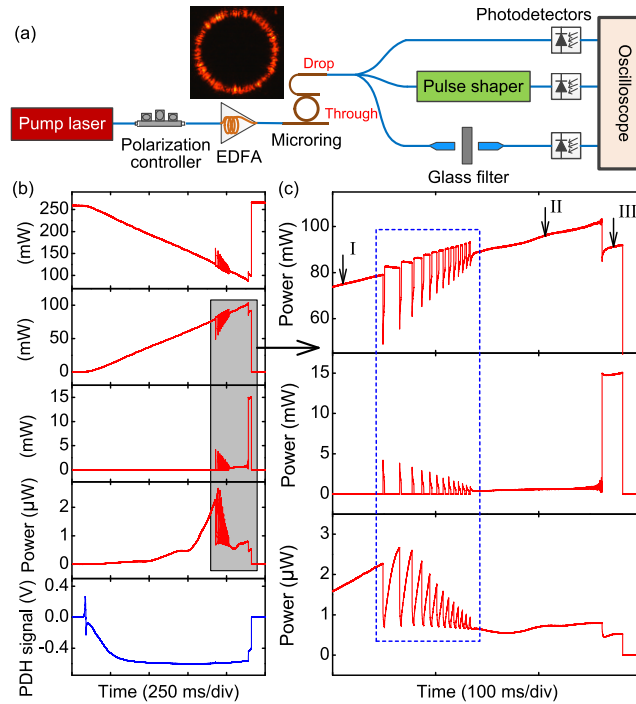


FIG. 1. Second-harmonic assisted comb generation in a normal-dispersion silicon nitride microring resonator. (a) Experimental setup. The inset shows the microscope image of the microring with second-harmonic radiation. (b) Transition curves when the pump laser scans across the resonance from shorter wavelength to longer wavelength. From top to bottom: total infrared (IR) power at the through port, total IR power at the drop port, IR comb power excluding the pump line at the drop port, second-harmonic power at the drop port, Pound–Drever–Hall (PDH) signal (the measurement setup is not shown in (a)). (c) Zoom-in details in the gray region marked in (b). The region marked in a blue dashed box shows a millisecond time scale oscillation. The drop-port comb spectra at different detuning stages (I, II, III) are shown in the following Fig. 2.

The optical power shows an oscillation in the region marked with a blue dashed box in Fig. 1(c). The oscillation occurs on a millisecond time scale and increases in speed as the pump laser is tuned to the red. Oscillation and self-pulsing caused by thermal nonlinearity has been observed in a variety of microresonator platforms [36]–[41]. It generally requires either two nonlinear mechanisms with different signs or two excited modes that interact with each other [36],[37]. For our microring, although two nonlinear processes with different response times were observed

previously in microheater actuated tuning experiments [42], the two processes appear to have the same sign. We believe the oscillation may involve the interplay between the pump and comb modes with a resonant mode at the second-harmonic frequency. As supporting evidence, we note that (i) switching of the comb power and second-harmonic power are both observed within the oscillation in Fig. 1(c), and (ii) we did not see the thermal oscillations when pumping resonances of the same microring that do not show second-harmonic generation – including those where we previously observed linear-mode-coupling initiation of the comb. In the current paper, we focus our investigations in the region where the oscillation vanishes with the pump laser further tuned to the red, and leave the development of a detailed oscillation model for future work.

The optical spectra measured in a range spanning more than one octave at different pump detunings are shown in Fig. 2(a). The zoom-in spectra of the fundamental and second-harmonic waves are shown in Figs. 2(b) and 2(c) respectively. Frequency combs can clearly be observed both around the IR pump as well as its second-harmonic. The comb formation can be divided into three different stages as follows. At detuning stage I (see Fig. 1(c)), only the second harmonic of the pump can be observed and no comb is generated. With the detuning changed to stage II, a narrow-band fundamental IR comb spaced by 1 FSR is generated and a few second-harmonic lines show up. The spacing between the second-harmonic lines is equal to that of the fundamental comb. The IR comb then transitions to a state with a much broader spectrum at detuning stage III. A slight change of the second-harmonic spectra is also observed in the transition. The IR comb shows very low intensity noise (below the noise background of the measuring electrical spectrum analyzer) in most part of the pump sweeping process, except in a small region right before transitioning to stage III where an increased intensity noise is observed. (The intensity noise is not revealed in the transmission curves in Fig. 1(c) due to a smoothing function of the oscilloscope; see Appendix A for traces captured with a different data acquisition mode.) Note that the low intensity noise of the broadband comb at stage III generally corresponds to mode-locking and formation of temporal structures in the cavity [14],[16]–[19].

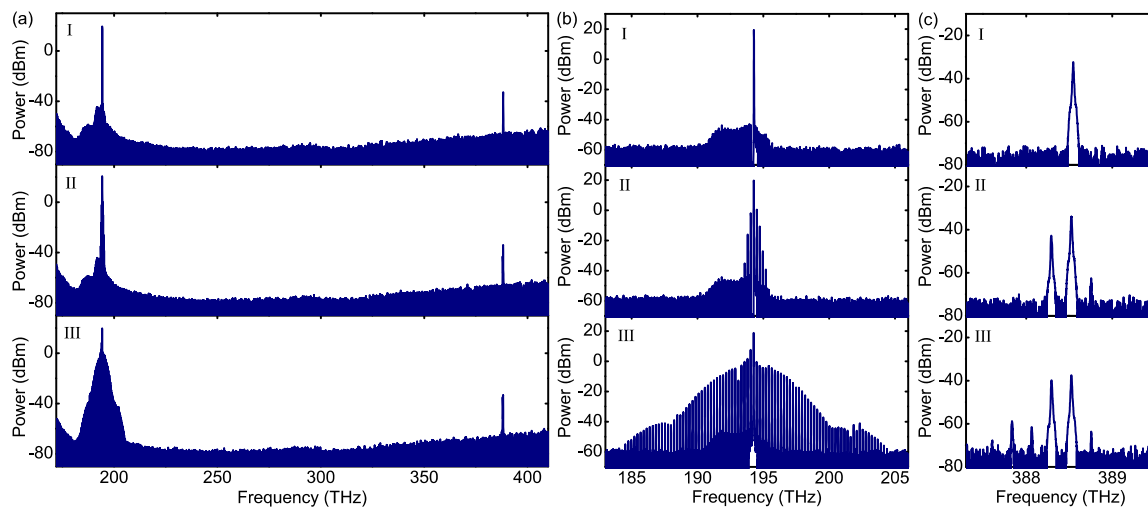


FIG. 2. Drop-port comb spectra at different detuning stages marked in Fig. 1(c). (a) Spectra measured in a range more than one octave. (b) Zoom-in infrared (IR) spectra. (c) Zoom-in second-harmonic spectra.

B. Time-domain characterization

To confirm the phase coherence of the broadband comb at stage III (and to investigate its time-domain characteristics) we have used spectral line-by-line shaping in combination with intensity correlation measurements [11],[12],[19],[21]. The dispersion of the fiber link between the output of the microring chip and the input of the intensity correlator is compensated; thus we can retrieve the comb spectral phase by compressing the comb to a transform-limited pulse. Figures 3(a) and 3(b) show respectively the amplitude and phase of the comb lines in the C-band (here the comb phase follows the sign convention generally used in ultrafast optics [43], i.e. the field of each comb line is represented by $Ae^{i(\omega t + \phi)}$ where A is the amplitude, ω is the angular frequency, and ϕ is the phase). The only difference between the optical fields at the through and drop ports is the complex amplitude of the pump line. All the comb lines at the drop port arise from coupling out of the microresonator. Therefore, the complex spectrum at the drop port should be the same as that in the cavity, as should the time-domain waveform. However, the pump line at the through port corresponds to the coherent superposition of the pump transmitted directly from the input waveguide and the pump component coupled out of the cavity. Because the complex pump field at the through port differs from that in the cavity, the time-domain waveforms at the through port and inside the cavity also differ [19]. For the specific example described here, the pump lines at the through and drop ports have very close power levels (difference <1 dB), but have a large phase difference (~ 2.4 rad). Figures 3(c) and 3(d) show the reconstructed waveforms at the through and drop ports respectively. The drop-port (intracavity) waveform is a dark pulse, which has been previously reported in normal-dispersion microresonators [19]. The dark pulse width is ~ 394 fs. Interestingly, the through-port waveform shows a nice bright pulse (width ~ 275 fs). Note that the bright pulse has a high background level which is limited by the cancellation ratio between the input pump and the dark pulse background in the through-port waveguide. The background level can be adjusted by changing the coupling condition between the microresonator and the through-port waveguide. Close-to-zero background can be achieved for the critical coupling condition. This way to tailor the pulse shape may be potentially useful for applications that require ultrashort bright pulses. Self-referenced cross-correlation is also measured to further verify the time-domain waveforms [19], and the results are consistent with those reconstructed through spectral line-by-line shaping (see Figs. 3(e) and 3(f)).

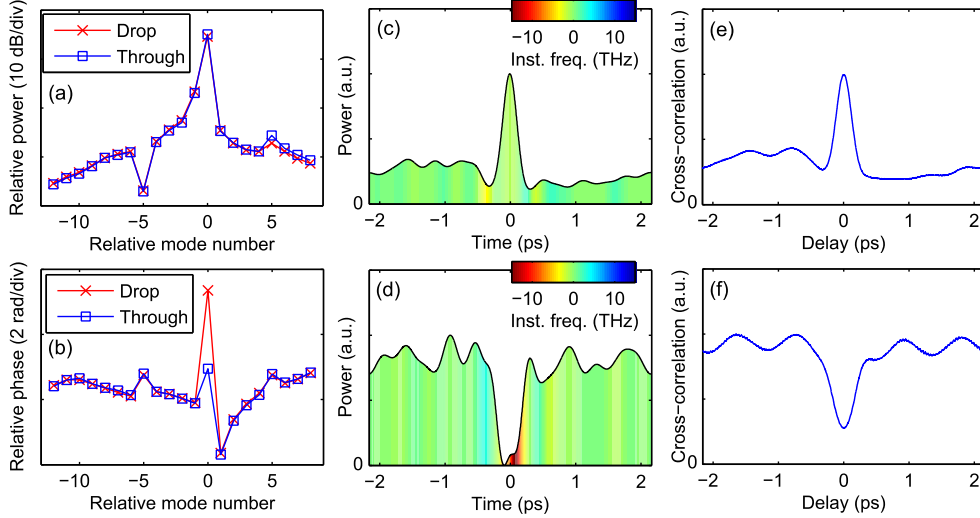


FIG. 3. Time-domain characterization of the broadband mode-locked comb at stage III. (a), (b) Amplitude and phase of the comb lines in the C-band. The amplitude of the pump line is very close at the through and drop ports, while a clear phase difference can be observed. (c), (d) Reconstructed waveforms at the through and drop ports, showing bright and dark pulses respectively. Inst. freq.: instantaneous frequency. (e), (f) Results of self-referenced cross-correlation which are consistent with (c), (d).

C. Hot-cavity detuning measurement

The normal dispersion microring we investigate here is the same ring we used in our previous paper [19]. In that work we showed that (i) the mode spectrum of the microring is perturbed by avoided mode crossings induced by linear coupling between transverse modes, and that (ii) the phase shifts associated with the linear coupling can enable comb generation, even in the normal dispersion regime, when pumping resonances around a mode crossing region. This mechanism cannot, however, explain the comb generation described here in the current paper. Indeed, a clear signature of linear mode coupling induced comb generation is that one of the initial comb sideband pair always grows from the resonance which is shifted from its natural frequency due to mode coupling [44]–[46]. In contrast, here the laser pumps a resonance 4-FSR (~ 7 nm) away from the mode crossing region; no frequency shifts due to mode coupling are observed for the resonances close to the pump from the cold-cavity dispersion profile, nor are linear mode coupling induced comb lines observed anywhere in the greater than one octave spectral measurement range. Of course, the mode crossing position may slightly shift in a hot cavity when the microresonator is pumped because different transverse modes may have different thermal shifting rates [19]. Thus to provide strong evidence that the comb generation we observe in Fig. 2 is not due to linear mode coupling in the hot cavity, the relative positions of the resonances in comb operation with respect to the comb lines (i.e. hot-cavity detuning) are measured.

A method of measuring the hot-cavity detuning by sweeping the frequency of a probe laser passed in the backward direction through the cavity was proposed in Ref. [21]. But this method is not suitable for our setup due to a strong backward reflection of the comb power from the

waveguide facet. Here we use an improved method based on fiber comb spectroscopy. The setup is shown in Fig. 4(a). A fiber frequency comb with a 20-MHz repetition rate is injected into the microring from the drop port via a circulator. The power of the fiber comb is adjusted such that it does not introduce any observable thermal and Kerr shifting. The fiber comb lines passing through the microring are gathered via another circulator at the pump input port. Meanwhile a fraction of the microcomb power is reflected to the backward direction from the waveguide facet and goes together with the fiber comb through the circulator (see the illustration in Fig. 4(a)). The fiber comb and microcomb lines from the circulator are combined with a tunable reference laser. Their radiofrequency (RF) beat notes are detected with a photodetector and analyzed with an electrical spectrum analyzer. To measure a specified resonance and the corresponding microcomb line, the frequency of the reference laser is tuned ~ 10 GHz lower than that of the microcomb line. The fiber comb lines pick up the shape of the microring transmission spectrum and then beat with the reference laser. The relative resonant frequency is obtained by fitting the intensities of the fiber comb lines with a Lorentzian function, while the relative frequency location of the microcomb line is determined directly from its beat note with the reference laser. The hot-cavity detuning, defined as the resonance frequency minus the pump (or comb line) frequency, can then be calculated as the resonance RF beat frequency minus the microcomb line RF beat frequency. Two example RF beat spectra indicating different detunings are shown in Fig. 4(b). The measurement accuracy of this method is estimated to be at the MHz level which is much smaller than the resonance width (~ 200 MHz).

The measured hot-cavity detuning results are shown in Fig. 4(c). All the comb lines including the pump are always blue detuned with respect to the resonances (i.e., resonance frequency $<$ frequency of pump or comb line, respectively). The detuning value is even larger than the resonance width. At stage III, the detuning versus wavelength shows as a quadratic function which indicates a normal group velocity dispersion of ~ 190 ps²/km, equal within experimental error to the dispersion measured for the cold cavity. The jump around 1535 nm is due to linear transverse mode coupling. Note that no detuning jumps are observed for the two resonances adjacent to the pump at either stage II or stage III. This is consistent with our conclusion that the 1-FSR comb at stage II in Fig. 2(b) is not due to linear mode coupling. Another interesting feature is that the hot-cavity detuning at stage II shows a linear slope versus wavelength superimposed onto the same quadratic function from stage III, suggesting a mismatch between the comb line spacing and the cavity FSR. To further verify this behavior, the comb line spacing is measured by using electro-optic down-mixing [47] and the results are shown in Fig. 4(d). The comb line spacing is changed by 212.7 MHz from stage II to stage III which agrees with the number retrieved from the detuning slope (214 MHz). Remarkably, all the key characteristics observed in experiments, i.e. the transition in the comb spectrum, as well as the abrupt change in comb line spacing, are accurately captured by numerical simulations based on a theoretical model that includes the second-order nonlinear interactions between the fundamental and second-harmonic waves. In particular, these simulations unequivocally reveal that the comb formation is triggered by the fundamental–second-harmonic interactions. The details of these simulations will be shown in the next section.

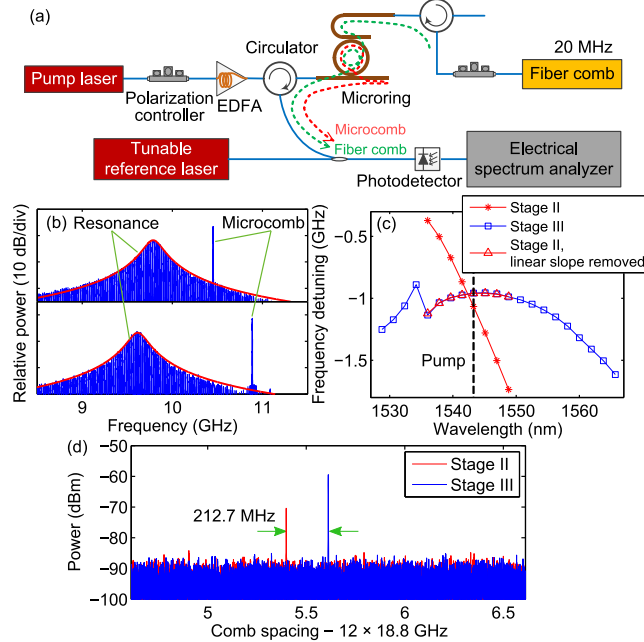


FIG. 4. Hot-cavity detuning measurement. (a) Experimental setup. The frequency of the reference laser is ~ 10 GHz lower than the microcomb line to be measured. (b) Example beat notes observed on the electrical spectrum analyzer. (c) Hot-cavity detuning defined as the resonance frequency minus the microcomb frequency. A change of the linear slope can be observed when the comb transitions from stage II to stage III, indicating a jump of the comb line spacing. (d) Measured microcomb beat note with electro-optic down-mixing, showing the comb line spacing jump.

III. NUMERICAL SIMULATION

In microresonators with only third-order Kerr nonlinearity, the evolution of the intracavity field can generally be described by the mean-field Lugiato–Lefever (L-L) equation [48],[49]. Note that modulational instability is absent in such a system when the group velocity dispersion is normal and when the pump laser is tuned from blue to red into the resonance as we do in our experiments [48]; thus no comb generation should be observed. (Although linear mode coupling may enable comb generation [19],[44]–[46], as we have explained above, our observations in the current experiment cannot be explained by this mechanism.) However, when there are simultaneous second- and third-order nonlinearities, a second-harmonic wave may be generated, with the fundamental and second-harmonic waves coupled to each other through second-order nonlinearity. The evolution of the intracavity fields in this case follows coupled L-L equations rather than the single L-L equation generally considered in Kerr comb generation. New dynamics may then arise which are responsible for the comb generation described in the current paper. To understand the underlying physics, a theoretical model incorporating coupled L-L equations is developed and numerical simulations are performed (see Appendix B.1 for the equation derivation [27],[28]). In particular, we find that the intracavity fields at the fundamental and the second-harmonic wavelengths obey the following coupled equations:

$$\frac{\partial E_1}{\partial z} = \left[-\alpha_1 - i\delta_1 - i\frac{k_1''}{2} \frac{\partial^2}{\partial \tau^2} + i\gamma_1 |E_1|^2 + i2\gamma_{12} |E_2|^2 \right] E_1 + i\kappa E_2 E_1^* + \eta_1 E_{\text{in}} \quad (1)$$

$$\frac{\partial E_2}{\partial z} = \left[-\alpha_2 - i2\delta_1 - i\Delta k - \Delta k' \frac{\partial}{\partial \tau} - i\frac{k_2''}{2} \frac{\partial^2}{\partial \tau^2} + i\gamma_2 |E_2|^2 + i2\gamma_{21} |E_1|^2 \right] E_2 + i\kappa^* E_1^2 \quad (2)$$

Here, E_1 and E_2 are the intracavity amplitudes of the fundamental and second-harmonic waves scaled such that $|E_{1,2}|^2$ represents the power flow; z is propagation distance in the cavity; τ is time; α_1 and α_2 are averaged loss per unit length including intrinsic loss and external coupling loss; δ_1 is related to the pump-resonance detuning by $\delta_1 = (\omega_0 - \omega_p)t_R/L$, with ω_0 resonance frequency, ω_p pump frequency, t_R round-trip time for the fundamental wave, L round-trip length; $k_1'' = d^2k/d\omega^2|_{\omega=\omega_p}$, $k_2'' = d^2k/d\omega^2|_{\omega=2\omega_p}$ group velocity dispersion; $\Delta k = 2k(\omega_p) - k(2\omega_p)$ phase mismatch; $\Delta k' = dk/d\omega|_{\omega=2\omega_p} - dk/d\omega|_{\omega=\omega_p}$ group velocity mismatch; γ_1 , γ_2 nonlinear coefficients of self-phase modulation; γ_{12} , γ_{21} nonlinear coefficients of cross-phase modulation; κ second-order coupling coefficient; $\eta_1 = \sqrt{\theta_1}/L$ coupling coefficient between the pump and the intracavity field where θ_1 is waveguide-resonator power coupling ratio for the fundamental wave; E_{in} amplitude of the pump.

Figure 5 shows the simulation results, which are very similar to our experimental observations (see Appendix B.2 for simulation parameters). The thermo-optic effect is not considered in the simulation. With the pump laser continuously tuned into the resonance from the blue side, a narrow-band fundamental comb is first generated, and then transitions to a much broader spectrum which corresponds to temporal dark pulse formation in the cavity. Detailed modulational instability analyses (Appendix B.2) show that, due to the second-order nonlinear interactions, the frequency modes of the fundamental wave are coupled to those of the second-harmonic wave, resulting in an effect similar to linear transverse mode coupling. Specifically, in the simulation example shown in Fig. 5, a close-to-phase-matching condition is achieved such that one comb sideband mode 1-FSR away from the pump is strongly coupled to its sum frequency with the pump through sum/difference frequency generation. The mode interaction gives rise to phase shifts that result in equivalent anomalous dispersion for the pump and the two adjacent fundamental modes. Modulational instability can thus occur, giving rise to the generation of a 1-FSR comb at stage II. The comb state becomes unstable in a small region right before transitioning to stage III, which is consistent with the experimental observation (see Appendix A). At this point we emphasize that, as expected based on the strong normal dispersion, no modulation instability (or comb formation) is observed in our simulations when the second-order nonlinearity is neglected ($\kappa=0$). This further confirms that it is precisely the nonlinear mode coupling that permits comb generation for our parameters.

The evolution of the fundamental intracavity waveform with the propagation distance is shown in Fig. 6. Note that the waveform at stage II shows a time drift which implies a deviation

between the comb line spacing and the cavity FSR. The shifting rate is $\Delta\tau = 5.04$ fs per round trip. The abrupt shift of the comb line spacing from stage II to stage III is then estimated as $\Delta\tau \cdot FSR^2 \approx 270$ MHz which is very close to the experimental result (212.7 MHz). The mismatch between the comb line spacing and the cavity FSR is caused by the second-harmonic mode coupling which introduces additional phase shifts to the comb lines when the fundamental wave propagates in the cavity. The additional phase shifts effectively shift the resonances seen by the comb lines resulting in an equivalent change of the local FSR. This effect is prominent at stage II (which achieves an effective anomalous dispersion for modulational instability), and gets weaker at stage III due to the transition to the broader mode-locked comb state.

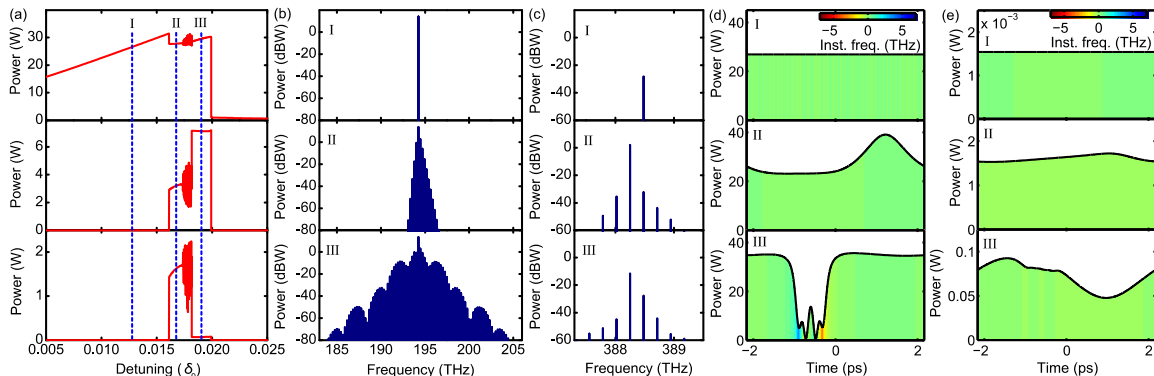


FIG. 5. Numerical simulation based on coupled L-L equations. (a) Intracavity power versus detuning ($\delta_0 = (\omega_0 - \omega_p)t_R$). From top to bottom: total fundamental power, fundamental comb power excluding the pump, total second-harmonic power. (b) Spectra of the fundamental wave at different detuning stages marked in (a). (c) Spectra of the second-harmonic wave. (d) Time-domain waveforms of the fundamental wave. Inst. freq.: instantaneous frequency. (e) Time-domain waveforms of the second-harmonic wave.

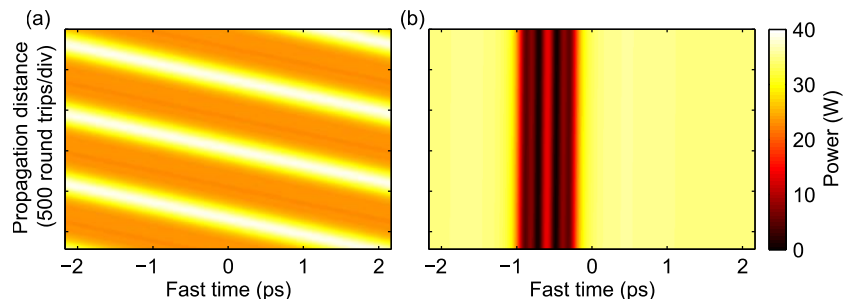


FIG. 6. Evolution of the intracavity fundamental wave with the propagation distance. (a) Stage II. (b) Stage III.

IV. DISCUSSION

Very interestingly, modulational instability and frequency comb generation in a cavity which contains purely second-order nonlinear medium have been demonstrated recently [26]–[28]. It should be noted, however, that the mechanism for comb initiation in our paper is different from that in Refs. [26]–[28]. In particular, in our setup the second-harmonic wave is relatively weak compared to the fundamental wave, such that the comb formation is still dominated by four-

wave-mixing due to the third-order Kerr effect. The role of the second-order nonlinearity is to induce phase-shifts around the fundamental frequency (through second-harmonic mode coupling), which enables phase-matching for four-wave mixing. In this sense, the second-order nonlinearity can be regarded as a perturbation to the general single L-L equation. In future, it is also highly interesting to pursue comb generation with much stronger second-order nonlinearity as has been partially investigated in numerical simulations [29].

The effect of second-harmonic mode coupling described here is similar to that of linear mode coupling, i.e. changing the local group velocity dispersion in microcomb generation. In the anomalous dispersion region, linear mode coupling has been found to prevent soliton formation when the mode coupling induced avoided crossing affects modes close to the pump [50]; in other cases, it may stabilize and organize multiple solitons to form soliton crystals [51]. We anticipate that similar behaviors can also happen with second-harmonic mode coupling. In the normal-dispersion region, however, second-harmonic mode coupling can be employed for spontaneous coherent comb generation as has been demonstrated here in this paper. It also provides a novel way of simultaneous comb formation and second-harmonic generation, which might prove especially important in the near-visible to visible range where several atomic transitions commonly used for stabilization of optical clocks are located [52] and where the large normal material dispersion is likely to dominate. This will potentially facilitate on-chip comb self-referencing for optical clocks and frequency metrology.

ACKNOWLEDGEMENTS

This work was supported in part by the National Science Foundation under grant ECCS-1509578, by the Air Force Office of Scientific Research under grant FA9550-15-1-0211, and by the DARPA PULSE program through grant W31P40-13-1-0018 from AMRDEC. Xiaoxiao Xue was supported in part by the National Natural Science Foundation of China under grant 61420106003. Miro Erkintalo acknowledges funding from the Marsden Fund and the Rutherford Discovery Fellowships of the Royal Society of New Zealand.

APPENDIX A: COMB INTENSITY NOISE

Figure 7 shows the evolution of the comb intensity noise with the pump detuning. The intensity noise is very low in most part of the pump scanning process, except in a small region right before transitioning to detuning stage III where an increased intensity noise is observed (Fig. 7(b) stage II+). The comb spectrum in the noisy region (Fig. 7(c)) is slightly wider than that at stage II (Fig. 2(b)). The noisy region is also observed in numerical simulations; see the transmission curves in Fig. 5(a). Figure 8(a) shows the evolution of the intracavity waveform with propagation distance in this region. It can be seen that the optical field becomes unstable. Figure 8(b) shows the averaged comb spectrum (as observed in experiments with a general slow-response optical spectrum analyzer) which is slightly wider than that of the noise-free comb at stage II (Fig. 5(b)).

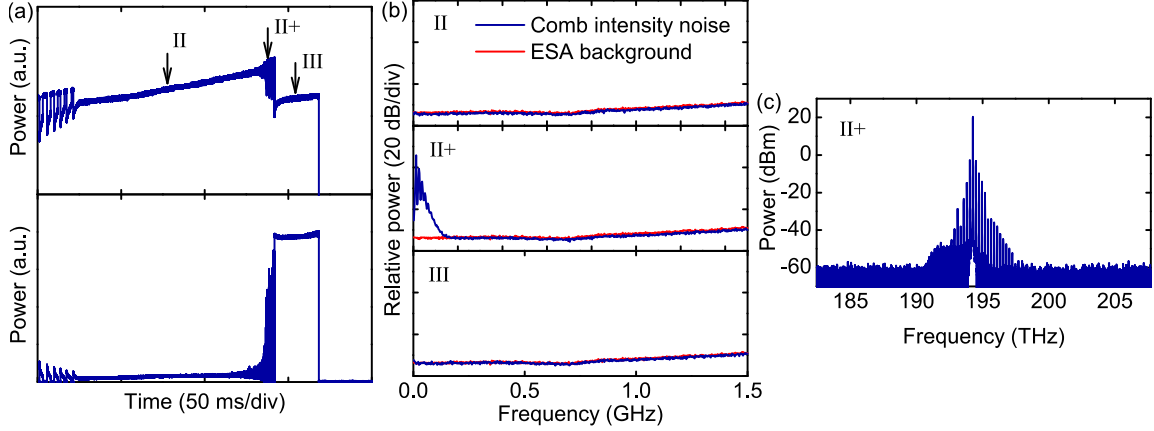


FIG. 7. Evolution of the comb intensity noise. The pump laser scans from shorter wavelength to longer wavelength at a speed of 0.5 nm/s. (a) Drop-port total power (upper) and comb power excluding the pump (lower), measured with the oscilloscope working in sampling mode. An increased intensity noise can be observed at detuning stage II+. (b) Comb intensity noise at different stages marked in (a). ESA: Electrical spectrum analyzer. (c) Fundamental comb spectrum at stage II+. The comb spectra at stages II and III are shown in Fig.2.

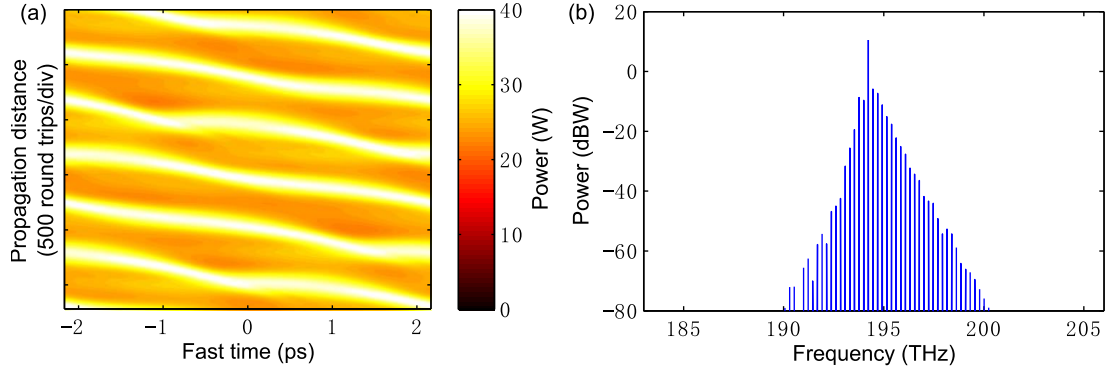


FIG. 8. Simulated comb in the noisy region right before transitioning to stage III. (a) Evolution of the intracavity waveform with propagation distance. (b) Averaged comb spectrum.

APPENDIX B: COUPLED LUGIATO–LEFEVER (L-L) EQUATIONS

1. Equation derivation

The fundamental and second-harmonic waves in the microresonator satisfy the following coupled equations [27],[28],[53]–[55]

$$\begin{aligned} \frac{\partial E_1}{\partial z} = & \left[-\alpha_{i1} - i \frac{k_1^*}{2} \frac{\partial^2}{\partial \tau^2} + i\gamma_1 |E_1|^2 + i2\gamma_{12} |E_2|^2 - \frac{\theta_1}{2} \sum_{n=-\infty}^{+\infty} \delta(z-nL) \right] E_1 + i\kappa E_2 E_1^* e^{-i\Delta k z} \\ & + \sum_{n=-\infty}^{+\infty} \delta(z-nL) \sqrt{\theta} E_m e^{i\delta_0 z/L} \end{aligned} \quad (3)$$

$$\frac{\partial E_2}{\partial z} = \left[-\alpha_{i2} - \Delta k' \frac{\partial}{\partial \tau} - i \frac{k_2''}{2} \frac{\partial^2}{\partial \tau^2} + i\gamma_2 |E_2|^2 + i2\gamma_{21} |E_1|^2 - \frac{\theta_2}{2} \sum_{n=-\infty}^{+\infty} \delta(z-nL) \right] E_2 + i\kappa^* E_1^2 e^{i\Delta k z} \quad (4)$$

Here, E_1 and E_2 are amplitude of the fundamental and second-harmonic waves scaled such that $|E_{1,2}|^2$ represents the power flow; z is propagation distance in the cavity; τ is time; α_{i1} and α_{i2} are amplitude loss per unit length; $k_1'' = d^2k/d\omega^2|_{\omega=\omega_p}$, $k_2'' = d^2k/d\omega^2|_{\omega=2\omega_p}$ group velocity dispersion; γ_1 , γ_2 nonlinear coefficients of self-phase modulation; γ_{12} , γ_{21} nonlinear coefficients of cross-phase modulation; θ_1 , θ_2 waveguide-resonator power coupling ratio; $\delta(\dots)$ delta function; L cavity round-trip length; $\Delta k = 2k(\omega_p) - k(2\omega_p)$ wave vector mismatch; $\Delta k' = dk/d\omega|_{\omega=2\omega_p} - dk/d\omega|_{\omega=\omega_p}$ group velocity mismatch; κ second-order coupling coefficient; E_{in} amplitude of the pump; $\delta_0 = (\omega_0 - \omega_p)t_R$ phase detuning where ω_0 resonance frequency, ω_p pump frequency, t_R round-trip time for the fundamental wave.

Note that the cavity boundary conditions are here represented by the discrete terms with delta functions. When the change of the intracavity field in one round-trip is very small (meaning that the cavity circumference is much smaller than the nonlinear length and dispersive length, and the cavity loss and pump detuning are very small), the discrete delta functions can be approximated by averaged continuous terms. Thus we get the following mean-field equations

$$\frac{\partial E_1}{\partial z} = \left[-\alpha_1 - i \frac{k_1''}{2} \frac{\partial^2}{\partial \tau^2} + i\gamma_1 |E_1|^2 + i2\gamma_{12} |E_2|^2 \right] E_1 + i\kappa E_2 E_1^* e^{-i\Delta k z} + \eta_1 E_{in} e^{i\delta_1 z} \quad (5)$$

$$\frac{\partial E_2}{\partial z} = \left[-\alpha_2 - \Delta k' \frac{\partial}{\partial \tau} - i \frac{k_2''}{2} \frac{\partial^2}{\partial \tau^2} + i\gamma_2 |E_2|^2 + i2\gamma_{21} |E_1|^2 \right] E_2 + i\kappa^* E_1^2 e^{i\Delta k z} \quad (6)$$

where $\delta_1 = \delta_0/L$, $\alpha_1 = \alpha_{i1} + \theta_1/(2L)$, $\alpha_2 = \alpha_{i2} + \theta_2/(2L)$, $\eta_1 = \sqrt{\theta_1}/L$. Then we do the following variable replacements.

With $E_1' = E_1 e^{-i\delta_1 z}$, $E_2' = E_2 e^{-i2\delta_1 z}$, we get

$$\frac{\partial E_1'}{\partial z} = \left[-\alpha_1 - i\delta_1 - i \frac{k_1''}{2} \frac{\partial^2}{\partial \tau^2} + i\gamma_1 |E_1'|^2 + i2\gamma_{12} |E_2'|^2 \right] E_1' + i\kappa E_2' E_1'^* e^{-i\Delta k z} + \eta_1 E_{in} \quad (7)$$

$$\frac{\partial E_2'}{\partial z} = \left[-\alpha_2 - i2\delta_1 - \Delta k' \frac{\partial}{\partial \tau} - i \frac{k_2''}{2} \frac{\partial^2}{\partial \tau^2} + i\gamma_2 |E_2'|^2 + i2\gamma_{21} |E_1'|^2 \right] E_2' + i\kappa^* E_1'^2 e^{i\Delta k z} \quad (8)$$

With $E_2'' = E_2' e^{-i\Delta k z}$, we get

$$\frac{\partial E_1'}{\partial z} = \left[-\alpha_1 - i\delta_1 - i\frac{k_1''}{2} \frac{\partial^2}{\partial \tau^2} + i\gamma_1 |E_1'|^2 + i2\gamma_{12} |E_2'|^2 \right] E_1' + i\kappa E_2'' E_1'^* + \eta_1 E_{in} \quad (9)$$

$$\frac{\partial E_2''}{\partial z} = \left[-\alpha_2 - i\Delta k - i2\delta_1 - \Delta k' \frac{\partial}{\partial \tau} - i\frac{k_2''}{2} \frac{\partial^2}{\partial \tau^2} + i\gamma_2 |E_2''|^2 + i2\gamma_{21} |E_1'|^2 \right] E_2'' + i\kappa^* E_1'^2 \quad (10)$$

To simplify the denotations, we still use E_1 and E_2 to represent the field amplitude in Eqs. (9) and (10). Then we get the mean-field coupled equations in the final form as Eqs. (1) and (2) in the main text.

2. Modulational instability due to second-harmonic mode coupling

Modulational instability analysis can be performed by applying a weak single-frequency perturbation to the continuous-wave (CW) solution of Eqs. (1) and (2) and investigating how the perturbation amplitude evolves with the propagation distance. In frequency domain, the perturbation corresponds to two modulation sidebands, i.e. upper and lower sidebands ($\omega_p \pm \omega$ where ω is the perturbation angular frequency). It is not easy to get analytic solutions of the modulational instability gain for the coupled L-L equations. Here we first qualitatively explain how modulational instability can be enabled by second-harmonic mode coupling in the normal-dispersion region, and then quantitatively calculate the modulational instability gain through numerical simulations. We focus on the situation in which the pump frequency and its second-harmonic line have some phase mismatch; thus the CW second-harmonic power is relatively weak compared to the pump. In this case, the second-harmonic mode coupling can be regarded as a perturbation to the general L-L equation that the fundamental wave follows; and the Kerr nonlinearity induced mixing between the second-harmonic modes can be neglected. The upper (lower) sideband of the fundamental wave is coupled to the upper (lower) sideband of the second-harmonic wave through sum/difference frequency generation (see Fig. 9), i.e.

$$\omega_p + (\omega_p \pm \omega) \rightarrow 2\omega_p \pm \omega \quad \text{and} \quad (2\omega_p \pm \omega) - \omega_p \rightarrow \omega_p \pm \omega.$$

When this process is close to phase-matched, an additional phase shift with the propagation distance will be introduced to the upper (lower) sideband mode of the fundamental wave due to the substantial photon exchange in sum/difference frequency generation. This effect is similar to that of linear mode coupling which causes mode splitting, meaning that the sideband mode involved is split to two compound modes with wave vectors different than that of the original mode without second-harmonic coupling. Then it is possible that one of the compound modes, the pump and the other sideband mode satisfy an equivalent anomalous dispersion, i.e. $k_{\omega_p+\omega}' - k_{\omega_p} - (k_{\omega_p} - k_{\omega_p-\omega}) < 0$ (here we suppose the upper sidebands are close to phase-matched; $k_{\omega_p+\omega}'$ represents the wave vector of the compound mode involved). Modulational instability will thus be enabled.

For the simulation results shown in Figs. 5 and 6 in the main text, the parameters are as follows: $\alpha_1 = 4.94 \text{ m}^{-1}$, $k_1'' = 186.9 \text{ ps}^2 \text{ km}^{-1}$, $\gamma_1 = 0.9 \text{ m}^{-1} \text{ W}^{-1}$, $\eta_1 = 3.07 \text{ m}^{-1}$, $\alpha_2 = 9.87 \text{ m}^{-1}$, $k_2'' = -151.6 \text{ ps}^2 \text{ km}^{-1}$, $\gamma_2 = 2.6 \text{ m}^{-1} \text{ W}^{-1}$, $\Delta k = -854.66 \text{ m}^{-1}$, $\Delta k' = 6.17 \times 10^{-10} \text{ s} \cdot \text{m}^{-1}$, $\gamma_{12} = 0.72 \text{ m}^{-1} \text{ W}^{-1}$, $\gamma_{21} = 1.44 \text{ m}^{-1} \text{ W}^{-1}$, $\kappa = 1.3 \text{ m}^{-1} \text{ W}^{-1/2}$, $FSR = 231.3 \text{ GHz}$, $E_{\text{in}} = 0.447 \text{ W}^{1/2}$. The propagation loss for the fundamental wave is extracted from the measured cavity quality factor in 1550-nm range. Due to the lack of a proper tunable laser source in 750-nm range, we cannot measure the quality factor for the second-harmonic wave. Thus we assume the loaded quality factor for the second-harmonic wave is half of that for the fundamental wave. The spatial mode for the fundamental wave is the fundamental transverse electric (TE) mode which is verified experimentally by measuring the polarization and cavity FSR. The spatial mode for the second-harmonic wave is investigated through numerical simulations using a commercial software *COMSOL*, and is found to be the 4th order TE mode which has the minimum phase mismatch with the fundamental wave (the second-harmonic phase matching wavelength is $\sim 1620 \text{ nm}$). The group velocity dispersion for the fundamental wave is measured with frequency comb assisted spectroscopy [56], while for the second-harmonic wave is obtained through numerical simulations. The self- and cross-phase modulation coefficients are calculated based on the simulated mode distributions. The nonlinear refractive index is $n_2 = 2.4 \times 10^{-19} \text{ m}^2 \text{ W}^{-1}$ [57]. Since the wave vector mismatch is very sensitive to the actual material dispersion, this parameter is freely tuned in our simulations. Another freely tuned parameter is the second-order coupling coefficient which is given by [58]

$$\kappa = \frac{2\varepsilon_0\omega_p d_{\text{eff}}}{4} \iint \left[E^{2\omega_p}(x, y) \right]^* \left[E^{\omega_p}(x, y) \right]^2 dx dy \quad (11)$$

where ε_0 is the vacuum permittivity; ω_p is angular frequency of the pump; $E^{2\omega_p}$ and E^{ω_p} are normalized field distribution such that $\frac{1}{2} \iint E \times H^* dx dy = 1$; $d_{\text{eff}} = \chi_{\text{eff}}^{(2)}/2$ and $\chi_{\text{eff}}^{(2)}$ is in the order of $10^{-12} \sim 10^{-11}$ which is in the range reported in literature [30]–[34].

Figure 10 shows the simulated modulational instability gain for detuning stage II in Fig. 5 ($\delta_0 = 1.67 \times 10^{-2}$). To run the simulation, a series of low-level probe sidebands is added to the CW fields and the coupled L-L equations are integrated with the split-step Fourier method. The evolution of the sideband amplitude is given by $A = A_0 e^{gL}$ where g is the net gain and L is the propagation distance. A narrow-band region with positive net gain is observed 1 FSR away from the pump, which is consistent with the 1-FSR comb generation observed in both experiments and simulations. The wave vector mismatch for sum/difference frequency generation involving the pump is also plotted. It can be found that the lower-sideband gain area is very close to phase-matched condition. This agrees with the second-harmonic mode coupling mechanism described above. The close-to-phase-match coupling for the lower sideband gives rise to a strong lower-sideband second-harmonic line which can be observed in both experiments and simulations (see Figs. 2(c) and 5(c)).

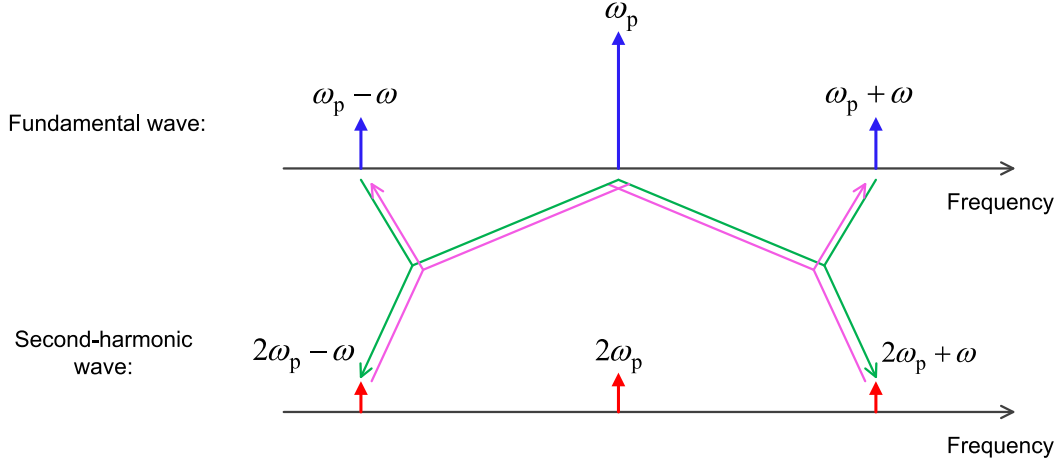


FIG. 9. Illustration of mode coupling through sum/difference frequency generation.

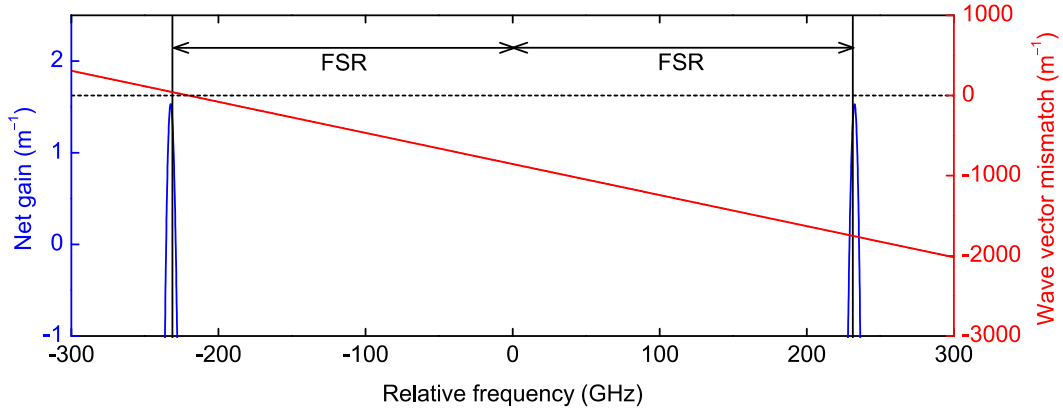


FIG. 10. Numerically simulated modulational instability gain for detuning stage II in Fig. 5. A narrow-band region with positive net gain can be observed 1 FSR away from the pump. The wave vector mismatch for sum/difference frequency generation, i.e. $k(\omega_p) + k(\omega_p + \omega) - k(2\omega_p + \omega) = \Delta k - \Delta k' \omega$, is also plotted. The lower-sideband gain area is very close to phase-matched condition.

REFERENCES

- [1] P. Del'Haye, A. Schliesser, O. Arcizet, T. Wilken, R. Holzwarth, and T. J. Kippenberg, *Optical frequency comb generation from a monolithic microresonator*, Nature **450**, 1214 (2007).
- [2] A. A. Savchenkov, A. B. Matsko, V. S. Ilchenko, I. Solomatine, D. Seidel, and L. Maleki, *Tunable optical frequency comb with a crystalline whispering gallery mode resonator*, Phys. Rev. Lett. **101**, 093902 (2008).
- [3] J. S. Levy, A. Gondarenko, M. A. Foster, A. C. Turner-Foster, A. L. Gaeta, and M. Lipson, *CMOS-compatible multiple-wavelength oscillator for on-chip optical interconnects*, Nature Photon. **4**, 37 (2010).

- [4] L. Razzari, D. Duchesne, M. Ferrera, R. Morandotti, S. Chu, B. E. Little, and D. J. Moss, *CMOS-compatible integrated optical hyper-parametric oscillator*, Nature Photon. **4**, 41 (2010).
- [5] I. S. Grudin, L. Baumgartel, and N. Yu, *Frequency comb from a microresonator with engineered spectrum*, Opt. Express **20**, 6604 (2012).
- [6] H. Jung, C. Xiong, K. Y. Fong, X. Zhang, and H. X. Tang, *Optical frequency comb generation from aluminum nitride microring resonator*, Opt. Lett. **38**, 2810 (2013).
- [7] B. J. M. Hausmann, I. Bulu, V. Venkataraman, P. Deotare, and M. Lončar, *Diamond nonlinear photonics*, Nature Photon. **8**, 369 (2014).
- [8] A. G. Griffith, R. K.W. Lau, J. Cardenas, Y. Okawachi, A. Mohanty, R. Fain, Y. H. D. Lee, M. Yu, C. T. Phare, C. B. Poitras *et al.*, *Silicon-chip mid-infrared frequency comb generation*, Nature Comm. **6**, 6299 (2015).
- [9] T. J. Kippenberg, R. Holzwarth, and S. A. Diddams, *Microresonator-based optical frequency combs*, Science **332**, 555 (2011).
- [10] A. B. Matsko, W. Liang, A. A. Savchenkov, and L. Maleki, *Chaotic dynamics of frequency combs generated with continuously pumped nonlinear microresonators*, Opt. Lett. **38**, 525 (2013).
- [11] F. Ferdous, H. Miao, D. E. Leaird, K. Srinivasan, J. Wang, L. Chen, L. T. Varghese, and A. M. Weiner, *Spectral line-by-line pulse shaping of on-chip microresonator frequency combs*, Nature Photon. **5**, 770 (2011).
- [12] S. B. Papp and S. A. Diddams, *Spectral and temporal characterization of a fusedquartz-microresonator optical frequency comb*, Phys. Rev. A **84**, 053833 (2011).
- [13] T. Herr, K. Hartinger, J. Riemensberger, C. Y. Wang, E. Gavartin, R. Holzwarth, M. L. Gorodetsky, and T. J. Kippenberg, *Universal formation dynamics and noise of Kerr-frequency combs in microresonators*, Nature Photon. **6**, 480 (2012).
- [14] K. Saha, Y. Okawachi, B. Shim, J. S. Levy, R. Salem, A. R. Johnson, M. A. Foster, M. R. E. Lamont, M. Lipson, and A. L. Gaeta, *Modelocking and femtosecond pulse generation in chip-based frequency combs*, Opt. Express **21**, 1335 (2013).
- [15] P. Del'Haye, K. Beha, S. B. Papp, and S. A. Diddams, *Self-injection locking and phase-locked states in microresonator-based optical frequency combs*, Phys. Rev. Lett. **112**, 043905 (2014).
- [16] S.-W. Huang, H. Zhou, J. Yang, J. F. McMillan, A. Matsko, M. Yu, D.-L. Kwong, L. Maleki, and C. W. Wong, *Mode-locked ultrashort pulse generation from on-chip normal dispersion microresonators*, Phys. Rev. Lett. **114**, 053901 (2015).
- [17] T. Herr, V. Brasch, J. D. Jost, C. Y. Wang, N. M. Kondratiev, M. L. Gorodetsky, and T. J. Kippenberg, *Temporal solitons in optical microresonators*, Nature Photon. **8**, 145 (2014).
- [18] X. Yi, Q.-F. Yang, K. Y. Yang, M.-G. Suh, and K. Vahala, *Soliton frequency comb at microwave rates in a high-Q silica microresonator*, Optica **2**, 1078 (2015).
- [19] X. Xue, Y. Xuan, Y. Liu, P.-H. Wang, S. Chen, J. Wang, D. E. Leaird, M. Qi, and A. M. Weiner, *Mode-locked dark pulse Kerr combs in normal-dispersion microresonators*, Nature Photon. **9**, 594 (2015).
- [20] A. Coillet, I. Balakireva, R. Henriet, K. Saleh, L. Larger, J. M. Dudley, C. R. Menyuk, and Y. K. Chembo, *Azimuthal Turing patterns, bright and dark cavity solitons in Kerr combs generated with whispering-gallery-mode resonators*, IEEE Photon. J. **5**, 6100409 (2013).

- [21] P. Del’Haye, A. Coillet, W. Loh, K. Beha, S. B. Papp, and S. A. Diddams, *Phase steps and resonator detuning measurements in microresonator frequency combs*, Nature Comm. **6**, 5668 (2015).
- [22] V. Brasch, M. Geiselmann, T. Herr, G. Lihachev, M. H. P. Pfeiffer, M. L. Gorodetsky, and T. J. Kippenberg, *Photonic chip-based optical frequency comb using soliton Cherenkov radiation*, Science **351**, 357 (2016).
- [23] S. Miller, K. Luke, Y. Okawachi, J. Cardenas, A. L. Gaeta, and M. Lipson, *On-chip frequency comb generation at visible wavelengths via simultaneous second- and third-order optical nonlinearities*, Opt. Express **22**, 26517 (2014).
- [24] H. Jung, R. Stoll, X. Guo, D. Fischer, and H. X. Tang, *Green, red, and IR frequency comb line generation from single IR pump in AlN microring resonator*, Optica **1**, 396 (2014).
- [25] Th. Udem, R. Holzwarth, and T. W. Hänsch, *Optical frequency metrology*, Nature **416**, 233 (2002).
- [26] I. Ricciardi, S. Mosca, M. Parisi, P. Maddaloni, L. Santamaria, P. De Natale, and M. De Rosa, *Frequency comb generation in quadratic nonlinear media*, Phys. Rev. A **91**, 063839 (2015).
- [27] F. Leo, T. Hansson, I. Ricciardi, M. De Rosa, S. Coen, S. Wabnitz, and M. Erkintalo, *Walk-off-induced modulation instability, temporal pattern formation, and frequency comb generation in cavity-enhanced second-harmonic generation*, Phys. Rev. Lett. **116**, 033901 (2016).
- [28] F. Leo, T. Hansson, I. Ricciardi, M. De Rosa, S. Coen, S. Wabnitz, and M. Erkintalo, *Frequency comb formation in doubly resonant second-harmonic generation*, Phys. Rev. A **93**, 043831 (2016).
- [29] T. Hansson, F. Leo, M. Erkintalo, J. Anthony, S. Coen, I. Ricciardi, M. De Rosa, and S. Wabnitz, *Single envelope equation modeling of multi-octave comb arrays in microresonators with quadratic and cubic nonlinearities*, J. Opt. Soc. Am. B **33**, 1207 (2016).
- [30] S. Lettieri, S. Di Finizio, P. Maddalena, V. Ballarini, and F. Giorgis, *Second-harmonic generation in amorphous silicon nitride microcavities*, Appl. Phys. Lett. **81**, 4706 (2002).
- [31] J. S. Levy, M. A. Foster, A. L. Gaeta, and M. Lipson, *Harmonic generation in silicon nitride ring resonators*, Opt. Express **19**, 11415 (2011).
- [32] T. Ning, H. Pietarinen, O. Hyvärinen, J. Simonen, G. Genty, and M. Kauranen, *Strong second-harmonic generation in silicon nitride films*, Appl. Phys. Lett. **100**, 161902 (2012).
- [33] T. Ning, H. Pietarinen, O. Hyvärinen, R. Kumar, T. Kaplas, M. Kauranen, and G. Genty, *Efficient second-harmonic generation in silicon nitride resonant waveguide gratings*, Opt. Lett. **37**, 4269 (2012).
- [34] A. Kitao, K. Imakita, I. Kawamura, and M. Fujii, *An investigation into second harmonic generation by Si-rich SiNx thin films deposited by RF sputtering over a wide range of Si concentrations*, J. Phys. D: Appl. Phys. **47**, 215101 (2014).
- [35] T. Carmon, L. Yang, and K. J. Vahala, *Dynamical thermal behavior and thermal self-stability of microcavities*, Opt. Express **12**, 4742 (2004).
- [36] M. L. Gorodetsky and V. S. Ilchenko, *Thermal nonlinear effects in optical whispering-gallery microresonators*, Laser Phys. **2**, 1004 (1992).
- [37] A. E. Fomin, M. L. Gorodetsky, I. S. Grudinin, and V. S. Ilchenko, *Nonstationary nonlinear effects in optical microspheres*, J. Opt. Soc. Am. B **22**, 459 (2005).

- [38] T. J. Johnson, M. Borselli, and O. Painter, *Self-induced optical modulation of the transmission through a high- Q silicon microdisk resonator*, Opt. Express **14**, 817 (2006).
- [39] L. He, Y.-F. Xiao, J. Zhu, S. K. Ozdemir, and L. Yang, *Oscillatory thermal dynamics in high- Q PDMS-coated silica toroidal microresonators*, Opt. Express **17**, 9571 (2009).
- [40] C. Baker, S. Stapfner, D. Parrain, S. Ducci, G. Leo, E. M. Weig, and I. Favero, *Optical instability and self-pulsing in silicon nitride whispering gallery resonators*, Opt. Express **20**, 29076 (2012).
- [41] L. Zhang, Y. Fei, Y. Cao, X. Lei, and S. Chen, *Experimental observations of thermo-optical bistability and self-pulsation in silicon microring resonators*, J. Opt. Soc. Am. B **31**, 201 (2014).
- [42] X. Xue, Y. Xuan, C. Wang, P.-H. Wang, Y. Liu, B. Niu, D. E. Leaird, M. Qi, and A. M. Weiner, *Thermal tuning of Kerr frequency combs in silicon nitride microring resonators*, Opt. Express **24**, 687 (2016).
- [43] A. M. Weiner, *Ultrafast Optics* (Wiley, 2009).
- [44] A. A. Savchenkov, A. B. Matsko, W. Liang, V. S. Ilchenko, D. Seidel, and L. Maleki, *Kerr frequency comb generation in overmoded resonators*, Opt. Express **20**, 27290 (2012).
- [45] Y. Liu, Y. Xuan, X. Xue, P.-H. Wang, S. Chen, A. J. Metcalf, J. Wang, D. E. Leaird, M. Qi, and A. M. Weiner, *Investigation of mode coupling in normal-dispersion silicon nitride microresonators for Kerr frequency comb generation*, Optica **1**, 137 (2014).
- [46] X. Xue, Y. Xuan, P.-H. Wang, Y. Liu, D. E. Leaird, M. Qi, and A. M. Weiner, *Normal-dispersion microcombs enabled by controllable mode interactions*, Laser Photon. Rev. **9**, L23 (2015).
- [47] P. Del'Haye, S. B. Papp, and S. A. Diddams, *Hybrid electro-optically modulated microcombs*, Phys. Rev. Lett. **109**, 263901 (2012).
- [48] M. Haelterman, S. Trillo, and S. Wabnitz, *Dissipative modulation instability in a nonlinear dispersive ring cavity*, Opt. Commun. **91**, 401 (1992).
- [49] S. Coen, H. G. Randle, T. Sylvestre, and M. Erkintalo, *Modeling of octavespanning Kerr frequency combs using a generalized mean-field Lugiato–Lefever model*, Opt. Lett. **38**, 37 (2013).
- [50] T. Herr, V. Brasch, J. D. Jost, I. Mirgorodskiy, G. Lihachev, M. L. Gorodetsky, and T. J. Kippenberg, *Mode spectrum and temporal soliton formation in optical microresonators*, Phys. Rev. Lett. **113**, 123901 (2014).
- [51] E. S. Lamb, D. C. Cole, P. Del'Haye, K. Y. Yang, K. J. Vahala, S. A. Diddams, and S. B. Papp, *Stabilizing multiple solitons in Kerr microresonator frequency combs*, In Conference on Lasers and Electro-optics 2016, SW1E.3, San Jose, CA.
- [52] A. D. Ludlow, M. M. Boyd, and J. Ye, *Optical atomic clocks*, Rev. Mod. Phys. **87**, 637 (2015).
- [53] G. P. Agrawal, *Nonlinear Fiber Optics* (Academic Press, 2001).
- [54] C. R. Menyuk, R. Schiek, and L. Tornert, *Solitary waves due to $\chi(2):\chi(2)$ cascading*, J. Opt. Soc. Am. B **11**, 2434 (1994).
- [55] A. V. Buryak, P. D. Trapani, D. V. Skryabin, and S. Trillo, *Optical solitons due to quadratic nonlinearities: from basic physics to futuristic applications*, Phys. Rep. **370**, 63 (2002).

- [56] P. Del'Haye, O. Arcizet, M. L. Gorodetsky, R. Holzwarth, and T. J. Kippenberg, *Frequency comb assisted diode laser spectroscopy for measurement of microcavity dispersion*, Nature Photon. **3**, 529 (2009).
- [57] K. Ikeda, R. E. Saperstein, N. Alic, and Y. Fainman, *Thermal and Kerr nonlinear properties of plasma-deposited silicon nitride/silicon dioxide waveguides*, Opt. Express **16**, 12987 (2008).
- [58] T. Suhara and M. Fujimura, *Waveguide Nonlinear Optic Devices* (Springer, 2003).